Description of mesoscale pattern formation in shallow convective cloud fields by using time-dependent Ginzburg-Landau and Swift-Hohenberg stochastic equations

Diana L. Monroy and Gerardo G. Naumis[*]

Departamento de Sistemas Complejos, Instituto de Física, Universidad Nacional Autónoma de México,
Apartado Postal 20-364, 01000, Ciudad de México, CDMX, Mexico

The time-dependent Ginzburg-Landau (or Allen-Cahn) equation and the Swift-Hohenberg equation, both added with a stochastic term, are proposed to describe cloud pattern formation and cloud regime phase transitions of shallow convective clouds organized in mesoscale systems. The starting point is the Hottovy-Stechmann linear spatiotemporal stochastic model for tropical precipitation, used to describe the dynamics of water vapor and tropical convection. By taking into account that shallow stratiform clouds are close to a self-organized criticality and that water vapor content is the order parameter, it is observed that sources must have nonlinear terms in the equation to include the dynamical feedback due to precipitation and evaporation. The nonlinear terms are derived by using the known mean field of the Ising model, as the Hottovy-Stechmann linear model presents the same probability distribution. The inclusion of this nonlinearity leads to a kind of time-dependent Ginzburg-Landau stochastic equation, originally used to describe superconductivity phases. By performing numerical simulations, pattern formation is observed. These patterns are better compared with real satellite observations than the pure linear model. This is done by comparing the spatial Fourier transform of real and numerical cloud fields. However, for highly ordered cellular convective phases, considered as a form of Rayleigh-Bénard convection in moist atmospheric air, the Ginzburg-Landau model does not allow us to reproduce such patterns. Therefore, a change in the form of the small-scale flux convergence term in the equation for moist atmospheric air is proposed. This allows us to derive a Swift-Hohenberg equation. In the case of closed cellular and roll convection, the resulting patterns are much more organized than the ones obtained from the Ginzburg-Landau equation and better reproduce satellite observations as, for example, horizontal convective fields.

I. INTRODUCTION

Convective clouds are well known to be crucial components of weather and climate, being a key process not only in the transport of heat, moisture, momentum, and dynamical quantities in the atmosphere but also by strongly affecting solar and long-wave radiation budgets from local to global scales [1,2]. Historically, most research involving convective clouds has focused on deep rather than shallow clouds. However, shallow convective clouds have significant impacts on the mesoscale as well as for large-scale atmospheric dynamics [3].

The study of shallow clouds is worthy for at least two reasons: First, they cool our planet reflecting a significant portion of the incoming solar radiation back to space contributing only marginally to the greenhouse effect, and, second, shallow clouds cover large fractions of our planet's subtropical oceans [2,4]. Even changes in the order of 1% in cloud cover or other properties may significantly affect the overall radiation balance [5]. As a consequence, cloud feedback influences significantly the response of the climate system to global warming [1,6].

Shallow clouds exhibit spatial organization over a wide range of scales [2,7]. Compared to spatially homogeneous low clouds, these modes of organization could be significant for the radiative effect of convective organization. They presumably affect the interaction of convection with atmospheric humidity and thus cloudiness plays a role in climate variability [8]. Cloud systems formed by shallow convection have horizontal dimensions ranging from several to 100 or 200 km. They are often characterized as mesoscale patterns [9] and are largely ignored in actual climate models [4].

Therefore, mesoscale systems need to be considered in climate-model parametrizations of the physical processes that affect the shallow cloud radiative response to climate perturbations [10]. At the same time, this is one of the challenges in climate sciences as contemporary climate models cannot resolve the length scales where it occurs [2]. Even the driving mechanisms responsible for these patterns are not completely well understood [11].

Stratocumulus clouds (Sc) are relevant examples of mesoscale organization of shallow convection on stratiform cloudiness. They have been studied in recent years due to their impact on the amount of sunlight reflected back to space [1,12]. Covering approximately one-fifth of Earth's surface in the annual mean, Sc are the dominant cloud type by area covered. Thus, there are few regions of the planet where these clouds are not climatologically important [13]. Sc are characterized by honeycomb-like patterns of stratiform cloudiness, arranged in either "open" or "closed" cells controlled by processes from the micrometer to the kilometer scale which interact in and above the scale O (10–100 km) of large-scale models [14].

---

*[*]naumis@fisica.unam.mx
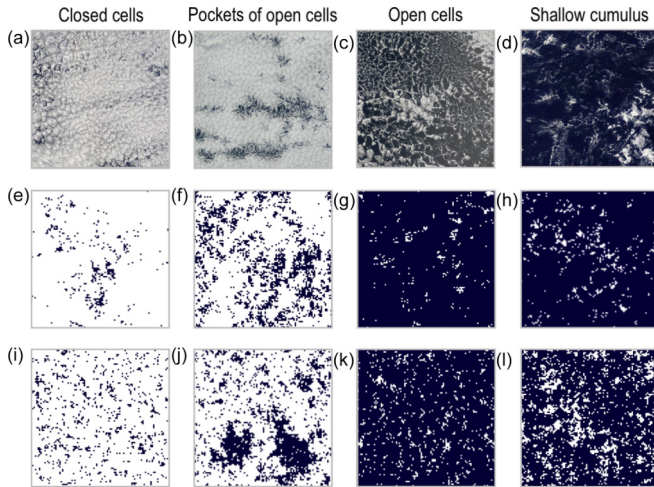
FIG. 1. The four distinctive phases of shallow cloud organization: closed-cell stratocumulus, pockets of open-cell stratocumulus, open-cell stratocumulus, and shallow cumulus viewed from satellite in panels (a) to (d), generated by the HS model [Eq. (3)] with the parameters proposed in Ref. [17] in panels (e) to (h) and by the nonlinear idealized model [Eq. (11)] in panels (i) to (l). See Appendix A for the parameter values. The data of the real fields were taken from the Moderate Resolution Imaging Spectroradiometer (MODIS) data and from the Geostationary Satellite Server (GOES) data from NOAA.

The organization of Sc into cellular or roll convection could be considered in first approximation as a form of Rayleigh-Bénard convection in the atmospheric boundary layer [15]. However, this mechanism does not completely explain the multiscale turbulent character of the mesoscale cloud convection (MCC) seen in observations, whereby other theories have been proposed to explain the driving of these patterns [16]. For Sc, in addition to the temperature difference between the lower boundary (the sea or land surface) and the upper boundary (a subsidence inversion), there are extra factors and processes whose interaction results in an enhancement or damping of the atmospheric convective circulation [14].

Many of those processes are key in Sc and MCC clouds: short-wave heating and long-wave cooling at cloud top, turbulence and entrainment, precipitation, latent heating, evaporative cooling and surface fluxes of energy as well as microphysical processes closely related with droplets concentration, aerosol effect and their influence in drizzle formation [13]. It is important to note the different processes involved in each regime. While open cells [Fig. 1(c)] appear as a consequence of descending motion and sinks of clear air at centers with ascending and cloudy air at their borders, closed cells [Fig. 1(a)] are formed in presence of upward motion and cloudy air in their centers and descending air at their interfaces. Heating from below is the key responsible process in open-cell convection when there is a large difference between sea surface temperature and air temperature; instead of that, radiative cooling of cloud tops is the key responsible process for closed-cell convection [13,14,18].

The transition from closed to open cellular convection is interesting from the system dynamics as well as from the

perspective of radiative forcing of the climate but is not clearly understood yet. Many theoretical and numerical models have been proposed. Two of the most investigated mechanisms are (1) cloud-aerosol-precipitation interactions [19] and (2) advection over warmer water [20–22]. The first approach can be thought of as microphysically driven and the second one as large-scale meteorologically driven. This last mechanism has been studied in recent years using satellite data, proposing a relationship between column-integrated water and precipitation rate as a self-organized criticality (SOC) [23] system. According to this, a critical value of water vapor (the tuning parameter) determines a nonequilibrium continuous phase transition to a regime of strong atmospheric convection with the emergence of precipitation (the order parameter) [24].

Based on these ideas, Hottovy and Stechmann proposed a linear stochastic equation to describe cloud phase transitions [25]. In this paper, we propose to modify such model by including a feedback mechanism for sources and sinks like precipitation or evaporation. This leads to a time-dependent stochastic Ginzburg-Landau equation and if convection is included, to a time-dependent stochastic Swift-Hohenberg equation. Such equations describe the formation and transition of stratocumulus cloud regimes: open cells, closed cells, and pockets of open cells [26] [Fig. 1(b)], as well as an unrobust phase [Fig. 1(d)] observed in shallow clouds. This mechanism for organized mesoscale convection simulates the transition to strong convection as a result of an increase in precipitation rate as a function of the column water vapor (CWV), in particular, for stratiform rain systems as Sc clouds [27]. By means of Fourier transforms, we compare the obtained patterns with several real cloud fields obtaining a good agreement.

In fact, the idea of developing a Ginzburg-Landau-type equation for cloud patterns is not completely new. In 2013, Craig and Mack proposed a Cahn-Hilliard equation to build a coarsening model for self-organization of tropical convection [28]. Their model started with the Allen-Cahn equation, which generalizes the Ginzburg-Landau equation to more general functionals [29]. As in our work, they used a similar order parameter, the tropospheric humidity, and a budget equation with feedback. They found a phase transition when the Landau-type functional has two minima, rather than one, leading to a bistable system with two equilibrium values of humidity [28]. Beyond the not so important differences in the type of Landau functional, the main departure from our work is that here we include stochastic terms in the equations. Thus, noise is considered in the time evolution, while in the work by Craig and Mack the noise is only used to produce an initial state [28]. As in other systems, noise has important effects in the pattern formation phase diagram [30,31].

The structure of this paper is the following, in Sec. II we detail the linear model while in Secs. III and IV the nonlinear models are introduced. Finally, the conclusions are given in Sec. V.

II. THE HOTTOVY AND STECHMANN LINEAR STOCHASTIC MODEL FOR MESOSCALE SHALLOW PATTERNS

In this section, we explain the basic details of the Hottovy and Stechmann (HS) model [25], based on an idealization of

water vapor dynamics as a stochastic diffusion process. In this model, several effects of the physical processes involved in cellular convection are included: evaporation, turbulent advection-diffusion of water vapor and precipitation.

The HS model [25] was proposed as a model for the dynamics of the cloudy boundary layer following the idealized simplification of models of phase transitions in other contexts. The model starts by considering the evolution of the total moisture content $q = q(\mathbf{r}, t)$ (water vapor plus condensed water, i.e., liquid and ice) in each planetary boundary layer column at a horizontal spatial location (x, y), normalized and shifted so that $q = 0$ represents the saturation level [17]. Spatiotemporal changes, given by the convective derivative of q, must be equal to the contribution of all sources and sinks such as precipitation or evaporation,

$$\frac{Dq}{Dt} = \frac{\partial q}{\partial t} + \mathbf{v} \cdot \boldsymbol{\nabla} q = S, \tag{1}$$

where $\mathbf{v}$ is the velocity. We next decompose q as $q = \bar{q} + q'$, where $\bar{q}$ is a large-scale average component and q' is a small fluctuation part, and in a similar way we decompose $\mathbf{v} = \bar{\mathbf{v}} + \mathbf{v}'$. Using Eq. (1), we obtain an equation for the large component [17],

$$\frac{\partial \bar{q}}{\partial t} = \bar{S} - \boldsymbol{\nabla} \cdot (\bar{q}\bar{\mathbf{v}}) - \boldsymbol{\nabla} \cdot (\overline{q'\mathbf{v}'}), \tag{2}$$

where it was used that $\bar{q}' = 0$ and $\overline{v}'_x = \overline{v}'_y = 0$. Next the small-scale flux convergence term $\boldsymbol{\nabla} \cdot (\overline{q'\mathbf{v}'})$ is approximated by a Laplacian $b\nabla^2 q$, used to represent eddy diffusion and mixing due to turbulence. The parameter b is an effective diffusion constant. The nonlinear turbulent effects contained in $\boldsymbol{\nabla}(\bar{q}\bar{\mathbf{v}})$ are taken into account by additional turbulent damping [32] $-\bar{q}/\tau_0$ and stochastic forcing, $D\dot{W}$ [33]. The term $\bar{q}/\tau_0$ represents a relaxation, where the parameter τ_0 is obtained through a careful analysis of the column-integrated water and precipitation rate [17]. The term $D\dot{W}$ represents a stochastic forcing, and is used as the simplest model for the turbulent fluctuations and others physical processes with a random component, such as the entrainment. Finally, the source term $\bar{S}$ represents the net water sources and sinks, including precipitation and evaporation of water from the ocean surface. It is considered to contribute with a constant and deterministic forcing F_0, and a partial stochastic contribution, taken already into account in the constant D.

Finally, the temporal evolution is given by the following equation [17]:

$$\frac{\partial q}{\partial t} = b\nabla^2 q - \frac{1}{\tau_0}q + F_0 + D\dot{W}, \tag{3}$$

where here, and to avoid overburden the notation, q represents the average part $\bar{q}$. In what follows, the same convention will be used.

It has been shown that this model can be translated into a spinlike Hamiltonian system that presents phase transitions [25] once q discretized using a function that takes the values 0 or 1 depending on the sign of q. Typical cloud fields obtained through numerical simulations using this equation are shown in Fig. 1. Therein, we include real images from satellite to provide a comparison. Although the model is able to reproduce the overall aspect of the fields and the phase tran-
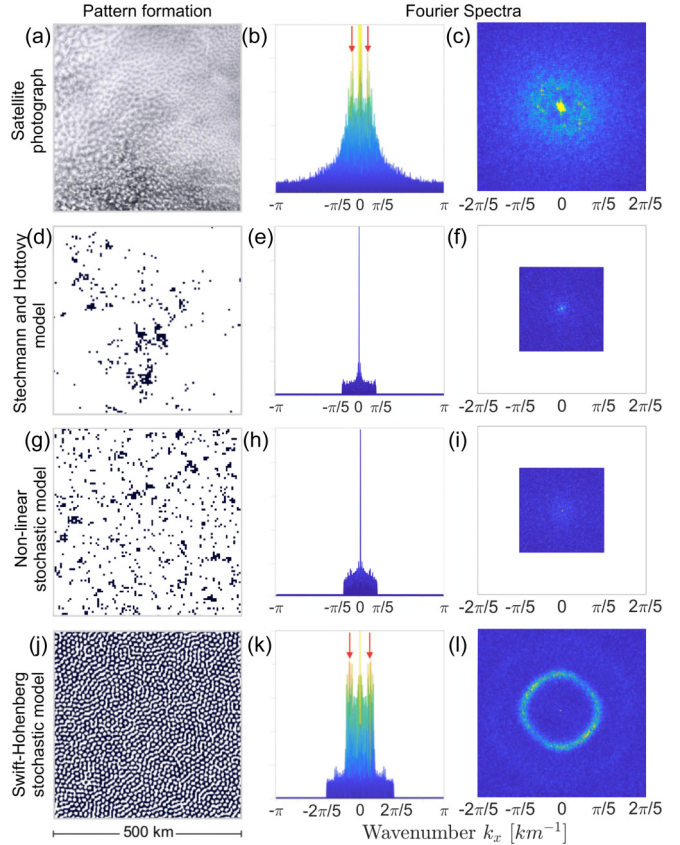
FIG. 2. Fourier transform of the closed-cell phase. Panels in the left column show the cellular pattern taken from (a) satellite photograph, (d) Hottovy and Stechmann model, (g) Ginzburg-Landau stochastic model and (j) Swift-Hohenberg stochastic model. In the central and right columns, we present the Fourier spectra of each pattern in the I/I_0-k_y plane and the orthogonal plane, respectively. We can identity in panels (b) and (c) and (k)–(l) a dominant frequency with radial symmetry indicated by red arrows, corresponding to a characteristic length of ≈ 14 km. The maximal spatial frequencies in panels (e), (h), and (k) are determined by the resolution of the grid used in the simulation given in the units of k_x (see text). See Appendix A for the parameter values. The simulations were done for $t = 1000$ h. The data of the real fields were taken from the MODIS data and the GOES data from NOAA.

sitions between them, it is also clear that there is much more organization in real cloud patterns for closed phases. To account for this, we have calculated the spatial Fourier transform of real closed-cell patterns taken from satellite photographs as well as from the outcome of HS model, as seen in Fig. 2.

In Figs. 2(b) and 2(c) we can identify one spatial frequency (wave vector) that reveals the existence of a particular structure. This is very clear in Fig. 2(c), in which a ringlike structure is observed. Nevertheless, in Figs. 2(e) and 2(f), we see that the Fourier transform of the outcomes obtained from the HS model does not show any characteristic dominant structure. This is expected as the HS is a linear model which does not couple modes [25].

Notice that in the case of the satellite photographs, we adjust the contrast and exposure of the original image—shown in Fig. 2(a)—before converting the grayscale image into a

binary image. This is done to define the cells with more details and precision.

Also, observe that in Figs. 2(e)–2(f), Figs. 2(h)–2(i), and Figs. 2(k)–2(j) there is a lower cut-off of the spectrum when compared with Figs. 2(b) and 2(c) and Figs. 2(k)–2(l). This is due to the resolution of the grid used. Although one can increase the cut-off frequency by growing the number of points in the simulation mesh, it turns out that the phases and parameters of the HS model depend on the mesh. On the other hand, decreasing the resolution of the real cloud fields leads to a lower-quality Fourier image. A trade-off is thus needed to keep the original parameters of the HS model and the best resolution of the real cloud fields. To solve this conundrum, here we adopted the policy of using absolute units in reciprocal space. These units are determined by the length ($L = 500$) in km of the real space field and the resolution of the photograph ($N_{\text{pixels}} \times N_{\text{pixels}} = 500 \times 500$), resulting in the cut-off frequency $k_x = \pm \pi N_{\text{pixels}}/L = \pm \pi$ (km^{-1}). For the simulation, the mesh has $N \times N$ points resulting in a cut-off frequency $k_x = \pm \pi N/L = \pm \pi (N/500)$ (km^{-1}). In all the Fourier transforms, the intensity I is scaled by the maximal intensity I_0.

III. NONLINEAR MODEL: TIME-DEPENDENT GINZBURG-LANDAU STOCHASTIC EQUATION

One of the most important points in the work of Craig and Mack and HS is the recognition of q as an order parameter [25,28]. In general, pattern formation is governed by order parameters whose spatiotemporal behavior is determined by nonlinear partial differential equations [34]. This suggests that the extra features seen in real cloud patterns are due to nonlinear effects. Following this idea, here we consider the cellular convective pattern described by a state vector $p(\mathbf{r}, t)$ which in this case corresponds to the cloud cover. Its evolution equation takes the general form of a partial differential equation [34]:

$$\frac{\partial p(\mathbf{r}, t)}{\partial t} = \mathbf{N}[\nabla, p(\mathbf{r}, t)], \tag{4}$$

where $\mathbf{N}$ denotes a nonlinear function. The behavior of the state vector $p(\mathbf{r}, t)$ of the pattern forming system can be represented as a functional of one or several order parameters, denoted by $\Phi(\mathbf{r}, t)$ that often can be directly related to a physical observable [34],

$$p(\mathbf{r}, t) = Q[\Phi(\mathbf{r}, t)],$$

where Q is a functional of $\Phi(\mathbf{r}, t)$. In order to recover the linear equation proposed by HS, in our model we identify $\Phi(\mathbf{r}, t) = q(\mathbf{r}, t)$, i.e., the CWV in each column of the lattice. Thus, instead of solving the determining equations for the state vector $p(\mathbf{r}, t)$, the spatiotemporal evolution is in general determined by an equation for the order parameter field [34]. The most simple case is the following:

$$\frac{\partial q}{\partial t} = L(\Delta)q + N[q]. \tag{5}$$

Here $L(\Delta)$ is a linear operator and $N[q, t]$ the nonlinear functional that is approximated by a polynomial expansion of q in its low-order derivatives.

Therefore, by comparing with Eq. (3) we can identify the operator $L(\Delta)$ with $\tau_0^{-1} + b\nabla^2$, while D and F_0 are parameters that determine the strength of the random and deterministic forcing generated by internal forcing due to small-scale cloud processes and large-scale external forcing, respectively. The transition of cloud area fraction (C_a) from a regime of closed cellular convection to a regime of pockets of open cells is determined by both parameters [7].

Let us start with the simple model given by Eq. (5) to indicate how nonlinear terms arise. We start by pointing out that several observational data and numerical studies have documented the crucial relationship between precipitation and water vapor for precipitation prediction in the context of convective parametrizations. Peters and Neelin [21,24] showed that there is a critical value q_c of the CWV where the mean precipitation $\langle P(q) \rangle$ increases rapidly as an approximate power law, i.e., $\langle P(q) \rangle \sim (q - q_c)^\beta$, for $q > q_c$. As $\beta < 1$, the precipitation variance has a strong peak at the critical value q_c and then diminishes [35–37].

It has been argued that the mechanism presents a tendency to self-maintain at criticality instead of being simply controlled by an external parameter [21,24]. In fact, SOC has been proposed to describe macroscopic critical phenomena such as organized structures associated with atmospheric convection [38].

This organization mechanism is supported by observations which exhibit that, even when the system hardly exceeds q_c, the CWV tends to decay more slowly than an exponential rate toward the higher values, reflecting the tendency toward SOC [14,24]. The same studies show a scale invariance suggesting a scaling law for atmospheric convection. Moreover, the invariance under spatial averaging suggests the applicability of the renormalization group, also supported by the SOC approach [14,24].

In the original HS model, the relaxation time τ_0^{-1} and the forcing F_0 were adjusted in such a way that different assumed models of the precipitation ratio fitted the results of Peters and Neelin for the precipitation conditional probability. If $r_{i,j}$ is the precipitation ratio for a cell with integer coordinates (i, j) in a square mesh, then there are two precipitation models, the first model is the Betts-Miller-like rain rate model [32],

$$r_{i,j} = |F_0|\sigma_{i,j}, \tag{6}$$

the other was provided by HS [17],

$$r_{i,j} = [|F_0| + q_{i,j}/\tau_0]\sigma_{i,j}, \tag{7}$$

where $\sigma_{i,j} = 1$ if $q > 0$ and $\sigma_{i,j} = 0$ otherwise. Notice that $\sigma_{i,j}$ is analogous to a spin variable. Its role is to signal whenever q is above the precipitation threshold $q = 0$. Then is possible to have rain.

While the conditional probability for precipitation can be obtained from the distribution function of q, *the linear model does not provide a feedback threshold due to precipitation in the source term $\bar{S}$*. In other words, the precipitation can be calculated a posteriori once the model is solved, but it does not enter into the calculation. We require $\bar{S}$ to depend on q.

Therefore, to improve the model one needs to include the fact that once the threshold for precipitation is reached, indicated by the spin variable $\sigma_{i,j}$, the source term will change. In fact, $\sigma_{i,j}$ can be used to derive an equivalent Ising Hamiltonian

for the cloud field [17]. Now comes the question, what is the most simple and natural choice for the feedback term? Following the Ising analogy, we can replace the spins $\sigma_{i,j}$ by the known Ising mean field, $\overline{\sigma} \approx [1 + \tanh(q/T)]/2$ with T a constant. Notice how the field is shifted to have $\sigma_{i,j} \approx \overline{\sigma} = 0$ for $q \to -\infty$ and $\overline{\sigma} = 1$ for $q \to \infty$. This results on two possible average precipitation rates $\overline{r}$ depending on the used model,

$$\overline{r} \approx \frac{1 + \tanh(q/T)}{2} |F_0| \tag{8}$$

or

$$\overline{r} \approx \frac{1 + \tanh(q/T)}{2} \left[|F_0| + \frac{q}{\tau_0} \right]. \tag{9}$$

As we are interested in the region around the threshold, i.e., near the lineal model, we can expand the hyperbolic tangent to obtain, using Eq. (8),

$$\overline{r} \approx \left[1 + \frac{q}{T} - \frac{1}{3} \left(\frac{q}{T} \right)^3 + \frac{2}{15} \left(\frac{q}{T} \right)^5 + \cdots \right] \frac{|F_0|}{2}. \tag{10}$$

Thus, we generated a nonlinear term able to model dynamically a precipitation threshold. Although in principle we can just modify the sources term in Eq. (3) by using $\bar{S} \to \bar{S} - \overline{r}$, it will be unwise not to recognize that sources must also depend dynamically on q, as for example, the conditional probability of having an increased q grows once precipitation occurs [39,40]. Thus, we left open the possibility of having an interplay between sources and sinks by the replacement $\bar{S} \to F_0 + D\dot{W} - \overline{r} + \overline{s}$ where $\overline{s}$ is an average dynamic source. The most simple model is to assume $\overline{s} \approx f\overline{r}$, where f controls the relative weight between sources, like evaporation, and precipitation. The parameter f allows an interplay between two kinds of nonlinear regimes, one dominated by sinks the other by sources.

Finally, we include, up to third order, the sources and sinks terms in Eq. (3) to obtain the following nonlinear model built from Eq. (8) Betts-Miller-like rain rate precipitation model,

$$\frac{\partial q}{\partial t} = b\nabla^2 q + Eq - Kq^3 \\ + D\dot{W} + F, \tag{11}$$

where the constants are given by

$$E = \frac{1}{\tau_s} - \frac{1}{\tau_0}, \quad K = \frac{1}{3\tau_s T^2}, \quad F = \left(\frac{f+1}{2} \right) |F_0| \tag{12}$$

with

$$\frac{1}{\tau_s} = \left(\frac{f-1}{2} \right) \frac{|F_0|}{T}. \tag{13}$$

The model given by Eq. (11) takes the same form of the celebrated time-dependent Ginzburg-Landau equation [41,42], now added with stochastic noise [43]. It is important to remark that Eq. (11) is also known as the stochastic Allen-Chan equation, as the order parameter is real, while in the Ginzburg-Landau equation it can be complex. Such equation coincides with the idea that most classical models for phase transitions are inherently nonlinear [44] and at the same time, satisfies one of the conditions of SOC: nonlinear interaction, normally

in the form of thresholds [45]. In Eq. (11), the threshold transition parameter T and the ratio f control the time parameter τ_s. This is a new characteristic time that competes with the damping time τ_0.

Also, we can use the alternative SH precipitation model given by Eq. (9). To terms of order q^3, we obtain a general model that contains the Ginzburg-Landau as a particular case,

$$\frac{\partial q}{\partial t} = b\nabla^2 q + \frac{q}{\tau_s} + Gq^2 - Kq^3 \\ + D\dot{W} + F, \tag{14}$$

where G defined as

$$G = \frac{f-1}{2T\tau_0}. \tag{15}$$

The main difference between Eqs. (11) and (14) is the quadratic term, which vanishes in the Betts-Miller-like rain rate model, resulting in the Ginzburg-Landau equation. As is well known, the quadratic term in the Ginzburg-Landau equation does not appear due to symmetry considerations. Here we will only study the Ginzburg-Landau equation, as the resulting pattern obtained from the second model were very different from real fields.

Figures 1(i)–1(l) shows the outcomes of the first model found solving numerically Eq. 11. Further details of the simulations are explained in the Appendices A and B, including several limiting cases studied to validate the software. In Fig. 2 we present the pattern and spectrum for the closed-cell phase. It is worthwhile mentioning that the spectra in Figs. 2(h)–2(i) were obtained from temporal and initial condition averages up to $t \approx 1000$ h. Although for the stationary regime of the Ginzburg-Landau (or Allen-Cahn) equation we reproduced the well-known behavior of a bell-shaped Fourier transform, for times $t < 100$ h and in some patterns we observed more structure in the nonlinear model when compared with the pure linear one (see next section and Appendix B). Observe that this is the most interesting regimen for real cloud patterns as typically they stay up to four days.

As was done previously with the linear model, in the following section we further compare the outcomes of our nonlinear model with the original clouds formations using Fourier spectrum and the closed-cell convection as reference.

A. Phase transitions diagrams

The model outputs in Figs. 1(e)–1(h) present the four phases of cloud organization shown in observational data from Figs. 1(a)– 1(d), respectively. It is possible to see the transition from closed-cells to pockets of open cells (POCs). These four cloud regimes correspond to four distinct parameter regimes of Eq. (11) where F and D are the tuning parameters which determine the phase transition.

Figure 3 presents the phase diagram for different patterns, obtained from the stochastic Ginzburg-Landau equation, in cases where they are qualitatively different as a function of the control parameters D and F. The control parameter values are similar to those found in the HS model, obtained through a careful tuning of the model with real data [25]. The only difference here is the constants E and K, which adjust the Fourier amplitude and position of the extra peaks. However,
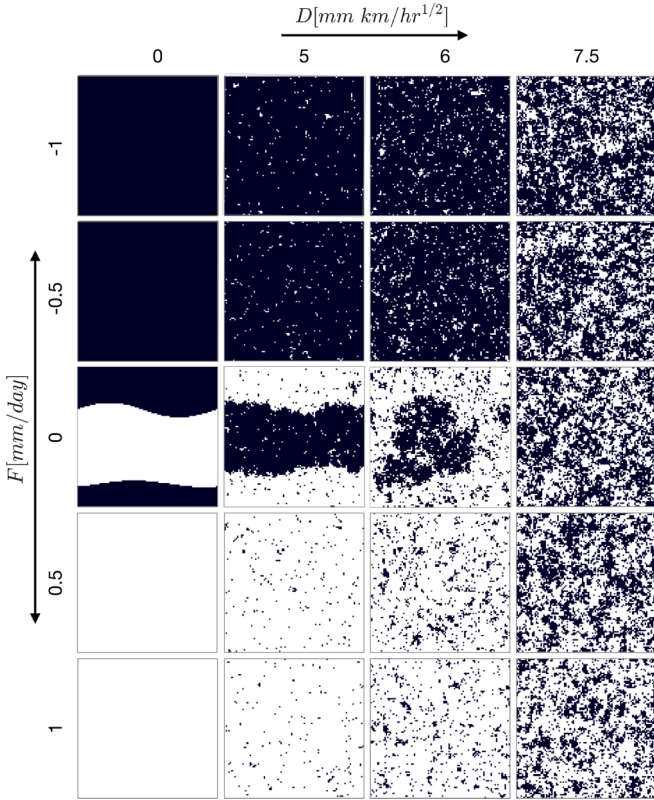
FIG. 3. Representative patterns obtained as a function of the control parameters D and F for the stochastic Ginzburg-Landau equation. For all the plots, we set $E = 1$ h^{-1} and $K = 1$ mm^2 h^{-1}. Notice that D and F have values in the same range of found by the original HS model from observational data [17]. These patterns were found at an intermediate relaxed regimen $t \approx 1000$ h and thus for $F \approx 0$ metastable banded patterns are seen.

FIG. 4. (a) Pattern formed by Fourier inverting the spectrum for the parameter values $F = 0$ and $D = 5$, as shown in Fig. 3. (b) A close up of the normalized spectrum in panel (a). The dominant frequency peaks are indicated by red arrows. (c) Pattern formed by inverting the central part of the spectrum shown inside the red frame in panel (b). (d) Pattern formed by inverting the external part of the spectrum shown inside green frames in panel (b).

as explained in Appendix A, these constants do not change for the different patterns, instead were fixed at $E = 1$ h^{-1} and $K = 1$ mm^2 h^{-1}.

It is important to remark in Fig. 3 that for $F \approx 0$, a banded pattern is seen. This is a typical intermediate transient state. It persist up to $t = 1000$ h. As F departs from $F = 0$, relaxation is faster and no structure is observed. Therefore, the spectrum in Fig. 2(h) does not present much structure. Its Fourier spectrum is a bell-shaped curve centered at $k = 0$, expected for such limiting cases. Other resulting patterns may have structure as in closed cells fields, but this only happens in the time regimen $t < 1000$ h, and eventually, the structure disappears.

As seen in Figs. 2(b) and 2(c), real patterns reveal the presence of a dominant frequency. This kind of spectrum is radially symmetric, implying that the corresponding structure is glasslike, as it has short-range order which is not preserved at long scales.

In Fig. 4 we present the Fourier spectrum for a nonrelaxed pattern for $F = 0$ and $t = 1000$ h. In Fig. 4(b), we present a zoom near $k = 0$, and which reveals two characteristic peaks. These peaks are not seen for a fully relaxed pattern of the stochastic Ginzburg-Landau or Cahn-Allen equation, which consists of a bell-shaped curve centered at $k = 0$. Such peaks

are only observed under nonperiodic boundary conditions or during transients. Notice that relaxation in the Allen-Cahn equation goes as a square root of the time and thus gets slower [46]. This is a typical result for systems with a double-well potential structure as there are two kinds of timescale dynamics [47,48].

Further verification of the transient nature of the peaks in Fig. 4 can be obtained by a reconstruction of the pattern by filtering out spatial frequencies higher than the main central peaks. The filtered spectrum can be used to reconstruct a pattern by an inverse Fourier transform, as seen in Fig. 4(c). Clearly, the peaks are due to the underlying transient banded state.

This metastable pattern lies in a special parameter region where noise and the nonlinear functional power are of the same order. In noise sustained patterns as in adaptive control algorithms, this region turns out to be the most interesting as it contains a lot more "structural" information [31]. As all benchmarks were reproduced for the limiting cases, including changes in the boundary conditions (see Appendix B), this means that the system is trapped in a deep metastable state.

In fact, numerically such mestastable patterns appear for $E + F > 0$ and its reason is easy to understand. The most simple stability analysis is obtained by linearization of the average field $q = \langle q \rangle$ in Eq. (11),

$$\frac{\partial \langle q \rangle}{\partial t} = b\nabla^2 \langle q \rangle + E\langle q \rangle + F. \qquad (16)$$

Considering a field, $\langle q \rangle = \delta q \exp(i\boldsymbol{k} \cdot \boldsymbol{r} + \lambda t)$ results in the condition,

$$\lambda = -bk^2 + (E + F). \tag{17}$$

The average field is stable whenever the real part of λ is such that $\text{Re}(\lambda) = E + F < 0$.

Therefore, for $t < 100$, the spatial structure for $F \approx 0$ corresponds to metastable states. As real cloud patterns are in this time regime, we can conclude that a possible outcome is that organization in the cloud pattern is due to a system trapped in a deep-basin metastable state. To understand this, we mention a clear analogy with glasses and crystals. Glasses are disordered solids in the observation timescale as they are not fully relaxed [49,50]. The low-free energy state corresponds to a crystal [51,52]. Yet we consider glasses and crystals as different physical entities.

Finally, it is worthwhile to mention that is well established numerically and mathematically that if the mesh size in the Ginzburg-Landau or Allen-Cahn equation simulation is shrunk, the numerical solutions would converge to a zero distribution with no pattern formation in the continuum limit [30,53]. In fact, the two-dimensional white noise-driven Allen-Cahn equation does not lead to the recovery of a physically meaningful limit [53]. A way to interpret the simulations of such equation is to view them as numerical approximations of equations driven by a noise field having a finite correlation length [30]. Here we used the mesh proposed by HS which has carefully tuned to reproduce meaningful physical results [17]. However, we verified that the mesh only has a small effect in the peak position for transient states, as the mesh is associated with much higher values of k and not at the center of the spectrum.

In the following subsection we further explore the pattern phase diagram of the system.

To further understand the changes between one and another phase, we use a phase diagram of cloud regimes using statistics moments as shown in Figs. 5 and 6. In the first diagram, the mean cloud area fraction ($\langle C_a \rangle$) is calculated as a function of D and F, i.e., $\langle \sigma \rangle = \langle \sigma(F, D) \rangle = \sum_{i,j} \sigma_{i,j}$ in the stationary state and by fixing τ_0 and b. Moreover, the plot in Fig. 6 provides the standard deviation, which is a measure of the statistical sensitivity.

In Fig. 5 is notorious the phase diagram regions belonging to each regime: the closed-cell regime corresponds to $F > 0$ and the open-cell regime corresponds to $F < 0$, as indicated by the mean C_a, since while the average value cloud area of open cells is 1, the mean of the closed ones is 0. On the other hand, the POCs could be seen in the middle of both regimes as their transition in the region around $F = 0$ with intermediate values of the mean C_a between 0 and 1. All these cellular regimens are associated with intermediate values of D. The shallow cumulus regime [Fig. 1(d)] appears for $D > 8$ mm h$^{-1/2}$ at all F values.

It is intuitive to understand why for small D, the C_a attains its mean unordered value: in this case, the value $\langle C_a \rangle = 1$ should be reached for positive F, and $\langle C_a \rangle = 0$ for negative F. However, higher values of E and K affect this picture (see below).
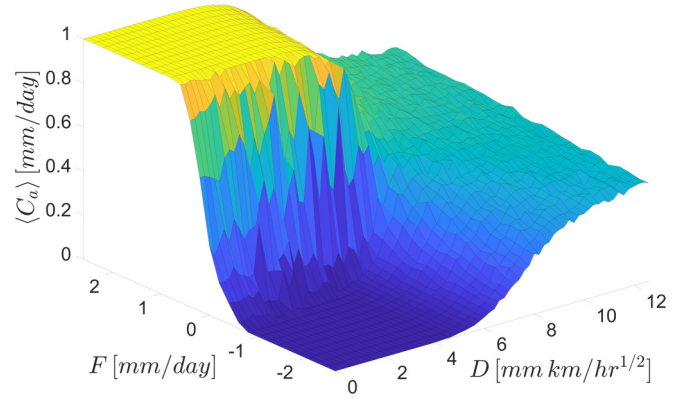
FIG. 5. Phase diagram of shallow cloud regimes for the Ginzburg-Landau nonlinear stochastic model given by Eq. (11). The plot shows the mean cloud area fraction ($\langle C_a \rangle$) as a function of variability, D, and the net source-sink parameter F. The transition from open to close cells is clearly seen as a transition from high to low values of the $\langle C_a \rangle$. However, this picture changes by increasing E and K, resulting in two limiting cases (see Appendix C).

Furthermore, to have a measure of the climate response or climate uncertainty, in Fig. 6 we present the standard deviation of the cloud area fraction ($S_d(C_a)$). The open and closed cellular regimes are associated with low values of the $S_d(C_a)$. The POCs and shallow phases are associated with high values of the $S_d(C_a)$, indicating how small changes in F or D lead to very large changes in $\langle C_a \rangle$. It also shows how the $S_d(C_a)$ increases drastically out of the regions where it presents the closed or open cellular patterns.

Finally, it's important to mention the effect of the E and K parameters on the phase diagram showed in Fig. 5. After a systematic tuning, we developed a phase transition with respect to these parameters, i.e., the change of the E and K values result in different phase spaces. Even when it is possible to recover the four regimes of interest, the F and D
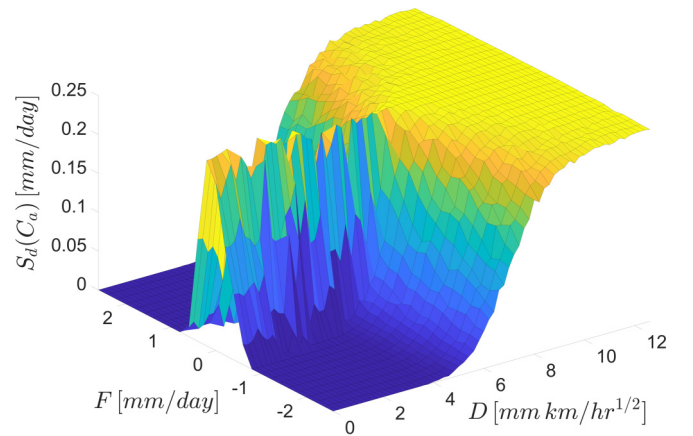
FIG. 6. Plot of the cloud area fraction standard deviation ($S_d(C_a)$) as a function of the variability, D, and net source-sink, F, for the Ginzburg-Landau stochastic model given by Eq. (11). The open and closed cellular regimes are associated with low values of the $S_d(C_a)$. The POCs and shallow phases are associated with high values of the $S_d(C_a)$.
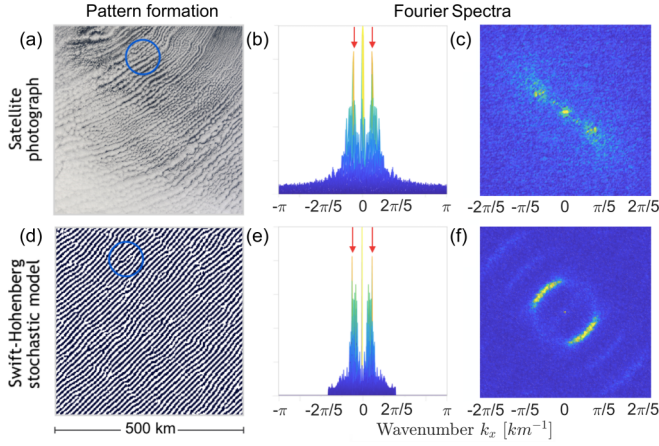
FIG. 7. Fourier transform of the horizontal convective rolls. Panels in the left column show the horizontal convection pattern taken from (a) satellite photograph and (d) the Swift-Hohenberg model given by Eq. (21). In the central and right columns, are presented the Fourier spectra in the I/I_0-k_y plane and the orthogonal plane, respectively. We can identity in panels (b) and (c) and then (e) and (f) a dominant frequency with axial symmetry indicated by red arrows. Notice that in panels (a) and (d), the blue circles indicate bifurcations observed in the real and simulated patterns. See Appendix A for the parameter values. The data of the real fields was taken from the MODIS data, and the GOES data from NOAA.

pairs able to form each phase vary considerably; we discuss an example in Appendix C. On the other hand, fixing F and D at the values used for the cellular regimes, we conclude that even when these phases could be formed, the dominant amplitudes in their Fourier spectra change for the effect of the E and K parameters. Understanding the physical interpretation of all these parameters and their full effect on cloud formation requires further study.

IV. STOCHASTIC SWIFT-HOHENBERG MODEL

In spite that the stochastic nonlinear models already show certain organization, Figs. 1(a) and 7(a) reveal that some real cloud fields still can be much more organized and in fact are in a different physical limit. They reveal hexagonal cells mimicking patterns arising from Rayleigh-Bénard convection. Indeed they are considered as a form of Rayleigh-Bénard convection in moist atmospheric air [22,54]. For such special cloud fields, we need to depart from some assumptions of the original HS model as after an exhaustive exploration of the parameters phase diagrams, there is no way to generate such highly ordered patterns. The dominant turbulent diffusion term prevents them to form. Returning to the budget equation (2), we see two possibilities. Either the source term or the small-scale flux convergence terms induce the selection of certain wavelengths. As clouds move, the pattern can persist in time, thus the source term is improbable to produce such behavior and we can keep our heuristically derived terms. The next natural step is to consider changes in the small-scale flux convergence term, i.e., in the operator $L(\Delta)$. The idea behind such change is the following. Suppose a pattern in which a wave-mode k_c is selected in an otherwise isotropic system. Let $\tilde{q} = \tilde{q}(k, t)$ be the Fourier transform of $q(r, t)$ in the space

domain. The leading-order dynamics must be of the following form:

$$\frac{\partial \tilde{q}}{\partial t} = (\alpha|\boldsymbol{k}|^2 - \beta|\boldsymbol{k}|^4 + \dots)\tilde{q}, \tag{18}$$

where $\alpha > 0$ and $\beta > 0$, as we require small-wavelength modes to decay, i.e., $\tilde{q}(\boldsymbol{k}, t) \to 0$ for $\boldsymbol{k} \to \infty$. In terms of the constants, the selected wave mode is given by $k_c = \sqrt{\alpha/2\beta}$. Transforming to real space, we are lead to the following general equation:

$$\frac{\partial q}{\partial t} = -\alpha\nabla^2 q - \beta(\nabla^2)^2 q. \tag{19}$$

We can take $\beta = 1$ as scale. Therefore $\alpha = 2k_c^2$ and we complete squares in Eq. (19),

$$\frac{\partial q}{\partial t} = \left[k_c^4 - \left(k_c^2 + \nabla^2\right)^2\right]q. \tag{20}$$

This procedure to find the operator works for many types of pattern-forming systems [55,56], but was first formally deduced from the Navier-Stokes equations in the Boussinesq approximation to study the effects of thermal fluctuations on a fluid near the Rayleigh-Bénard instability [57]. By considering the expansion of $N[q]$ in Eq. (14) and collecting the linear terms in q using a constant $\epsilon = k_c^4 + 1/\tau_s$, we obtain the following stochastic equation:

$$\frac{\partial q}{\partial t} = \left[\epsilon - \left(k_c^2 + \nabla^2\right)^2\right]q + Gq^2 - Kq^3 + F + D\dot{W}, \tag{21}$$

which is the stochastic Swift-Hohenberg equation. The solutions of Eq. (21) are still in the process of being investigated [58] although studies of the Swift-Hohenberg equation in the presence of noise started decades ago [59].

Equation (21) can be solved numerically through implicit finite differences and a successive over-relaxation (SOR) method as proposed by Pérez-Moreno *et al.* [60]. In Fig. 2(j) and Fig. 7(d) we show the formation of two particular patterns that arise in the Rayleigh-Bénard convection, hexagons and rolls. Further details of the simulations are explained in Appendix A. Both patterns have been identified as ways of organization in Sc clouds and their formation depends on the parameter G that controls the strength of the quadratic nonlinearity. In Figs. 2(a) and 2(j) and in Figs. 7(a) and 7(d) we compare satellite photographs with simulations of hexagons and rolls, respectively; we can see clear similarities with the satellite patterns. To confirm the similarities, the Fourier spectrums of the real and simulated cloud formations were performed.

In Figs. 2(b) and 2(c) and Figs. 2(k)–2(l), the hexagonal pattern spectrum reveals the presence of a dominant frequency for a cut along a certain direction. In Fig. 2 we can identify a principal frequency and other harmonics of lower amplitude. This coincides with the spectrum of a cellular pattern with defects and not highly ordered as a result of the forcing added in Eq. (21), which generates different sizes of cells without a particular tessellation. On the other hand, in Figs. 7(b) and 7(c) and Figs. 7(e) and 7(f) we show the presence of a dominant frequency with axial symmetry that corresponds to a pattern formed by parallel rolls in real space. In both kinds

of convection, the simulations recover the structures formed in real cloud fields.

V. CONCLUSIONS

Following the work of Hottovy and Stechmann, we proposed a nonlinear differential equation for an order parameter field given by the column water vapor $q(\mathbf{r}, t)$ to describe the transitions of various pattern formations in mesoscale shallow clouds systems. One of the main modifications introduced to the original linear model is the possibility of a feedback due to sources. In particular, we used two precipitation rate models, one leading to a time-dependent stochastic Ginzburg-Landau equation while the other adds a quadratic term to this equation. The first model produces some realistic cloud fields and even glasslike patterns, i.e., with short-range order which is not preserved at long scales.

However, this model is not able to reproduce the highly ordered fields present in Rayleigh-Bénard convection in moist atmospheric air featuring rolls and hexagonal waves. Therefore, in the spirit of perturbation theory, we introduced a change in the small-scale flux convergence term, resulting in a stochastic Swift-Hohenberg equation, proposed here as a simple model for cloud fields. The numerical simulations confirmed the presence of closed-cellular and horizontal convection phases.

The success of both models can be appreciated by observing the real patterns in Fig. 1. Therein, we identified that the three patterns corresponding to MCC are not in a perfectly hexagonal arrangement (highly ordered) nor are they arranged in complete randomness (highly disordered). The distributions of cumulus, both in closed and open-cells, appear in some arrangement between these two extremes.

Both proposed nonlinear models are closer to this dominant structure than the linear one, while the Swift-Hohenberg equation allows the formation of clearly organized patterns for two characteristic convective regimes. Finally, we presented a phase diagram for the cloud patterns, using as basic parameters those found by HS by fitting the data, as well as additional nonlinear parameters we identified by comparing with the spatial Fourier, transforms of the patterns.

APPENDIX A: PATTERN PARAMETERS

1. The Stechmann and Hottovy linear stochastic model for mesoscale shallow patterns

In Figs. 1(a)–1(d), the outcomes of Eq. (3) were numerically solved using implicit finite differences with the same parameter values proposed by Hottovy and Stechmann [17,25]. A two-dimensional discrete spatial grid in a domain of L by L, where $L = 500$ km divided in a N by N lattice with $N = 100$ and lattice spacing of $\Delta x = \Delta y = 5$ km; this was chosen to be roughly the smallest width of individual cells of tropical deep convection. The boundary and initial conditions were considered periodic and random, respectively. It was defined $q_{i,j}(t)$ as the integrated CWV and $W_{i,j}(t)$ as independent white noise, denoted formally as the derivative of a Wiener process [17,25], in the (i, j)th column of the atmosphere for $i, j = 1, \ldots, N$.

The parameters b and τ_0 conserves the values $b = 25$ km^2 h^{-1} and $\tau_0 = 100$ h, as proposed by HS [17,25]. In each phase of Fig. 1, the parameter values used were [Fig. 1(a)] $D = 1.55$ mm h$^{-1/2}$, $F = 0.12$ mm day^{-1}; [Fig. 1(b)] $D = 1.94$ mm h$^{-1/2}$, $F = 0.048$) mm day^{-1}; [Figs. 1(c)] $D = 1.55$ mm h$^{-1/2}$, $F = -0.12$ mm day^{-1}; and [Fig. 1(d)] $D = 11.62$ mm h$^{-1/2}$, $F = -0.72$ mm day^{-1}.

2. Nonlinear model: Time-dependent Ginzburg-Landau stochastic equation

In Figs. 1(i)–1(j), the outcomes of Eq. (11) were obtained using the same domain and discretization as well as initial and boundary conditions of the linear model simulations. The parameters b and τ_0 conserves the same values proposed by Hottovy and Stechmann [17,25], while different values of F and D, in the same range used by them ($F_0 \sim \pm 1$ mm day^{-1} and $D \sim 10$ mm h$^{-1/2}$), were explored to find the regimens observed in Figs. 1(i)–1(l). The dynamics of the nonlinear terms in Eq. (11) was determined by the parameters E and K whose values, after an exploration of different orders of magnitude, were fixed in $E = 1$ h^{-1} and $K = 1$ mm^2 h^{-1}. The increase of both parameters is associated with a major percolation in the boundaries around open or closed clusters to the same F and D values.

In particular, the parameter values used in Fig. 1 for Eq. (11) were [Fig. 1(i)] $D = 6$ mm h$^{-1/2}$, $F = 1$ mm day^{-1}; [Fig. 1(j)] $D = 9$ mm h$^{-1/2}$, $F = 0.2$ mm day^{-1}; [Fig. 1(k)] $D = 6$ mm h$^{-1/2}$, $F = -1$ mm day^{-1}; and [Fig. 1(l)] $D = 10.25$ mm hr$^{-1/2}$, $F = -0.4$ mm day^{-1}.

3. Stochastic Swift-Hohenberg model

In Fig. 2(g) and Fig. 7(c) we show the formation of two particular patterns that arise in the Rayleigh-Bénard convection, hexagons and rolls. Eq. (21) was solved numerically through implicit finite differences and a SOR method as proposed by Pérez-Moreno *et al.* [60].

For such simulations, the numerical method used a two-dimensional discrete spatial grid in a domain of L by L, where $L = 500$ km was divided in a N by N lattice with $N = 200$ and lattice spacing of $\Delta x = \Delta y = 2.5$ km. In this case, this discretization was chosen to approximate the cell diameter of the real ones. The boundary and initial conditions were
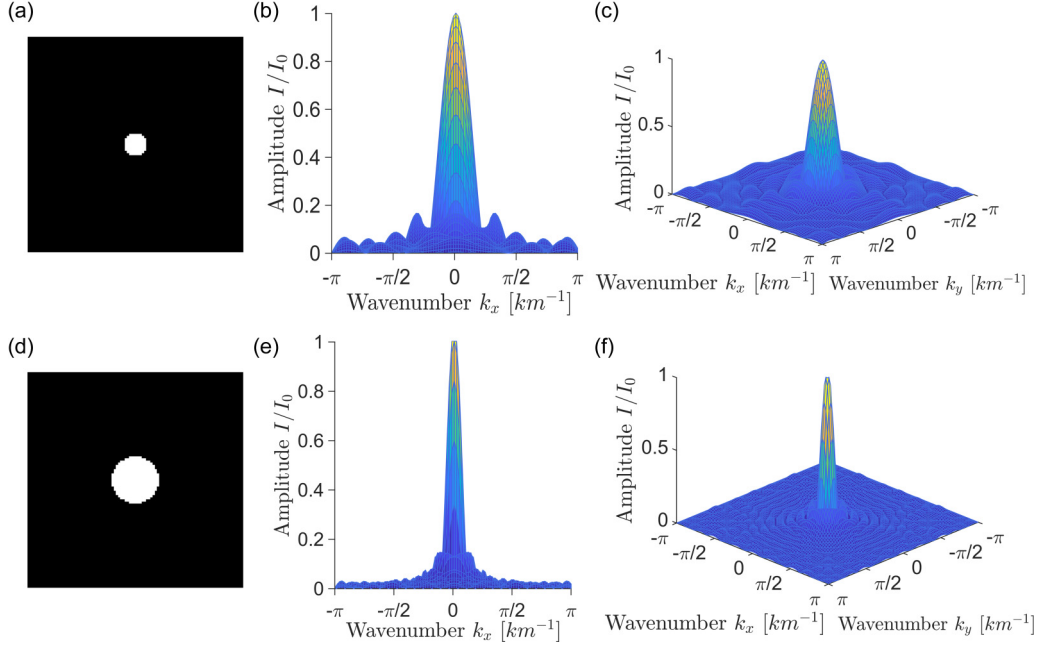
FIG. 8. Fourier transform code proof. (a) Circle with radio $r = 20$ pixels in a 200×200 square lattice, the corresponding two-dimensional Fourier transform is shown in (b) the I/I_0-k_y plane and (c) the orthogonal plane. Panels (d), (b), and (e) are equivalent to (a), (b), and (c) to a circle with radio $r = 50$ pixels in a 200×200 square lattice.

considered again as periodic and random. In the SOR method, it was used as the iteration step $k = 15$ and as the relaxation factor $w = 1.3$.

To form each pattern, the parameters were fixed as follows: in Fig. 2(g) $\epsilon = 0.1$, $k_c = 1.3$ km^{-1}, $g = 1$, $D = 0.15$ mm km h$^{-1/2}$, $F = 0.1$ mm day^{-1} and in Fig. 7(c) $\epsilon = 0.3$, $k_c = 1.2$ m^{-1}, $g = 0$, $D = 0.3$ mm km h$^{-1/2}$, $F = 0.25$ mm day^{-1}.

APPENDIX B: FOURIER TRANSFORM ANALYSIS

To investigate the validity and accuracy of the main text results, in this section we present first, in subsection 1, the Fourier Transform software testing and second, in subsections 2, 3, and 4 an examination of the numerical method used to solve the Eq. (11) varying time averages, mesh grid, and boundary conditions. Note that, in subsections 2, 3, and 4, the spectra present only a section of the amplitude domains in order to make it easier to identify the wave numbers that appear as a reminiscence of the characteristic metastables states of the Ginzburg-Landau patterns formed when $F \approx 0$.

1. Fourier transform benchmarks

First, we tested the Fourier spectrum software using known examples to reproduce the expected results. Among the targets, the most simple one is two circular apertures with different diameters, as shown in Figs. 8(a) and 8(d). In the middle and right columns, the respective Fourier spectrum of each aperture is shown in Figs. 8(b) and 8(e) the I/I_0-k_y plane and in Figs. 8(c) and 8(f) the orthogonal plane. The analysis is in perfect agreement with the expected analytical results.

2. Time-averaged Fourier transform

We next investigate the persistence of the dominant wave numbers that appear in the Ginzburg-Landau Fourier spectra for times $t \approx 100$ h. For this purpose, we computed the time-averaged Fourier spectra of the four distinctive cloud phases generated by the Ginzburg-Landau stochastic model (see Fig. 9) once the patterns reach a stationary state.

The corresponding two-dimensional Fourier transform of each phase was averaged over 20 independent simulations in the total period [150, 350] h at time intervals of $t_n = 10n + T_i$ for n an integer. The initial time, $T_i = 150$ h, corresponds to the common minimum time in which the four phases reach the stability according to the $\langle q(\mathbf{r}, t) \rangle$ value.

We conclude that these characteristic wave numbers are persistent for intermediate times $t \approx 100$ h, although may vanish at long times $t \approx 1000$ h, as can be verified in the phase diagrams that appear in the main text. As the dynamics of the Cahn-Allen slows down as a square root of the time, the
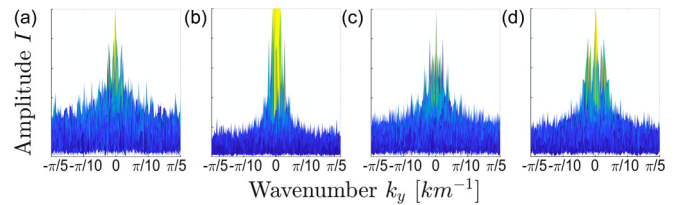
FIG. 9. The corresponding time-averaged Fourier transforms for the four distinctive phases of shallow cloud organization generated by the Ginzburg-Landau stochastic model [Eq. (11)] with the same order and parameters used in Figs. 10(e)–10(h). The Fourier transforms were averaged over 20 independent simulations (from $t = 100$ to $t = 300$ each 10 time steps).
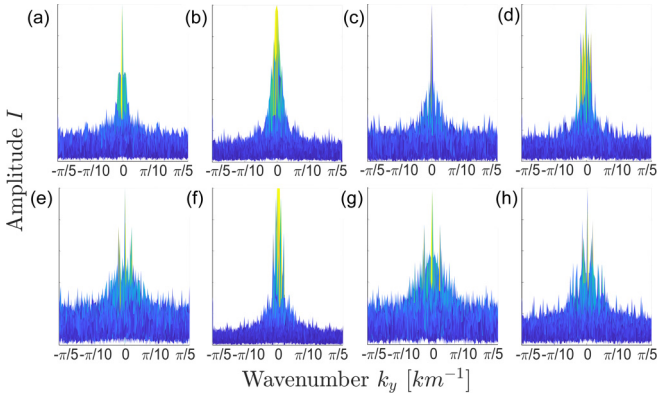
FIG. 10. Fourier transforms for the four distinctive phases of shallow cloud organization at the time regimen $t \approx 100$ h: closed-cell stratocumulus, pockets of open-cell stratocumulus, open-cell stratocumulus, and shallow cumulus generated by the HS model [Eq. (3)] with the parameters proposed in Ref. [17] in panels (a) to (d) and by the Ginzburg-Landau model [Eq. (11)] in panels (e) to (h). See Appendix A for the parameter values.

characteristic wave numbers correspond to metastable states with a long decay time. We recognize that this is possibly equivalent to metastability presented in the two-dimensional Ising model under the effects of an external magnetic field.

3. Comparison between Hottovy-Stechmann and Ginzburg-Landau Fourier spectra

Once we had evidence of the Fourier spectra validity used in the analysis of the patterns, we investigate the role of nonlinear terms of the Ginzburg-Landau model in the emergence of patterns for certain couples of F and D parameter values. Figure 10 shows the Fourier transform corresponding to the four cloud phases of interest generated by the Hottovy-Stechmann model, in Figs. 1(a)–1(d), and by the Ginzburg-Landau model, in Figs. 1(e)–1(h), all taken in the time regimen $t \approx 100$ h.

The Fourier transforms in the top row show no dominant wave numbers over the rest, which is consistent with the lack of organization in the Hottovy-Stechmann patterns. However, the bottom row presents, as the Fig. 9 does, characteristic wave numbers that give the first clue of a more homogeneous distribution and so, more organization in the patterns formed by the Ginzburg-Landau model. Also, the fact that these dominant wave numbers appear only in the cellular phases allows to complement the phase diagrams in the main text to understand the effect of the tuning parameters, F and D, in the formation and transition of cloud phases.

4. Characterizing the effect of boundary conditions and mesh grid on Ginzburg-Landau Fourier spectra

Most of the numerical studies which have been found disordered spatiotemporal regimes formed by nonlinear partial differential equations have been done considering periodic boundary conditions, with the idea that in the limit of very large systems, the boundary conditions would not influence the system dynamics. However, for the description of real systems, it is necessary a systematic study of boundary con-
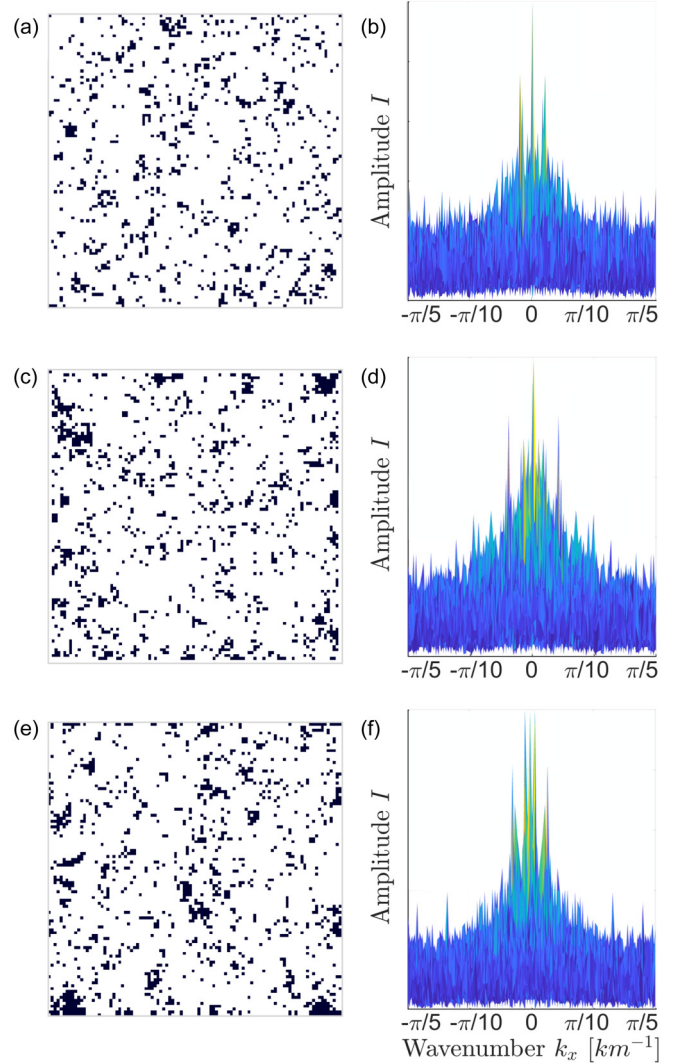
FIG. 11. Fourier transforms of the closed-cell phase at the intermediate time regimen $t \approx 100$ h. Panels in the left column show the closed cellular pattern taken from Ginzburg-Landau stochastic model [Eq. (11)] using (a) periodic boundary conditions, (c) Dirichlet boundary conditions, and (e) Neumann boundary conditions. In the right column, we present the corresponding Fourier spectrum of each pattern.

ditions to consider their possible effects in the formation of more realistic patterns.

For this reason, once we prove the validity of the Fourier transform program as well as the numerical solution of Ginzburg-Landau model, in this section we will focus on the behavior of the stochastic Ginzburg-Landau equation on different mesh refinement and with different types of boundary conditions.

First, through the comparison of periodic, Neumann and Dirichlet boundary conditions (see Fig. 11) we summarize the behavior observed numerically on the closed-cellular regimen formed in a two-dimensional rectangular domain under the same parameters detailed in Appendix A.

Applying null Dirichlet ($q = 0$), and Neumann ($\frac{\partial q}{\partial n} = 0$) boundary conditions, in the left column of Fig. 11 we show
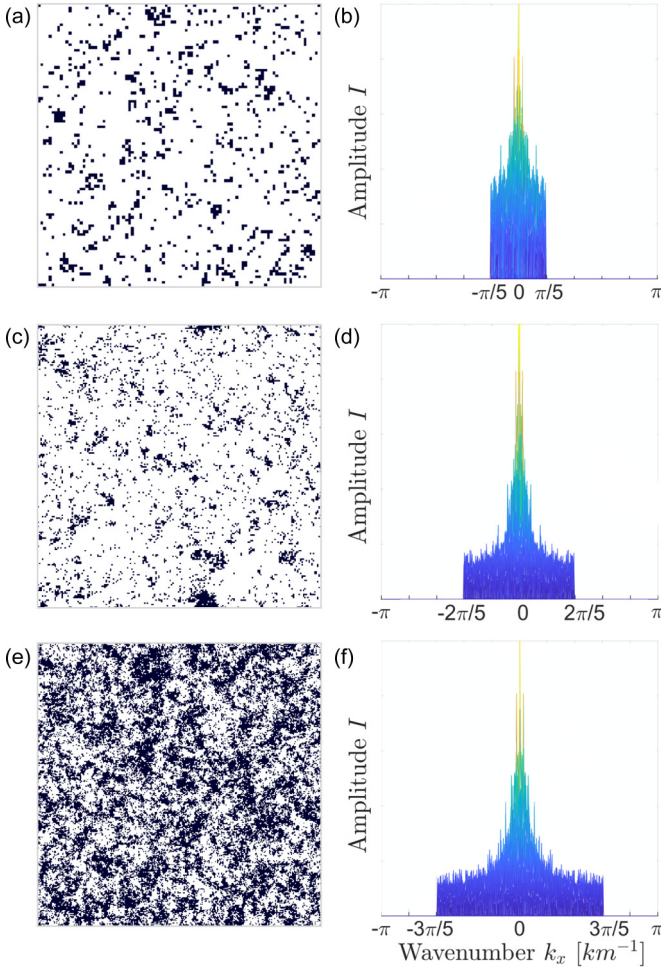
FIG. 12. Fourier transform of the closed-cell phase at the time regimen $t \approx 100$ h. Panels in the left column show the closed cellular pattern taken from Ginzburg-Landau stochastic model [Eq. (11)] solved in a square discrete domain of L by L, with $L = 500$ km, divided in a $N \times N$ lattice with (a) $N = 100$, (b) $N = 200$ and $N = 300$. In the right column, we present the corresponding Fourier spectrum of each pattern. The maximal spatial frequencies in panels (b), (d), and (e) are determined by the resolution of the grid used in the simulation given in the units of k_x.

the patterns formed under each kind of condition. In the right column, we can see their respective Fourier spectra. For the three cases, the spectra reveal similarities between them. In the left panels, it is possible to appreciate such behavior qualitatively. However, for the Dirichlet and Neumann cases, near to the walls, we can see open regions in contradistinction to the periodic case.

On the other hand, to investigate the effects of the mesh refinement on pattern formation, we simulate our system with the same initial and periodic boundary conditions specified in Appendix A over a square domain with side $L = 500$ km. In Fig. 12 we present the results for different mesh refinements $\Delta(x) = L/N$ where N is the number of lateral divisions in [Fig. 12(a)], $N = 100$, [Fig. 12(c)] $N = 200$, and [Fig. 12(e)] $N = 300$ cells. By observation of the left column is clear that $\Delta(x)$ affects the C_a; particularly, in Fig. 12(e), this is visible with the apparition of open regions and the decrease of the
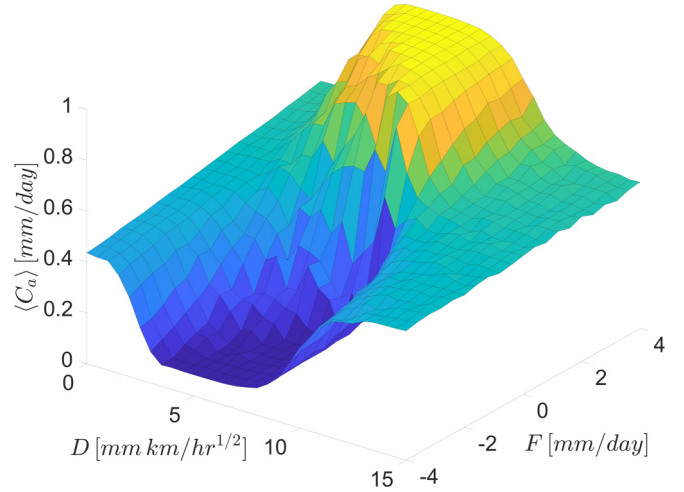
FIG. 13. Phase diagram of shallow cloud regimes for the Ginzburg-Landau stochastic model given by Eq. (11). The plot shows the mean cloud area fraction ($\langle C_a \rangle$) as a function of D and F fixing the parameters $E = 8.5$ h^{-1} and $K = 6.5$ mm^2 h^{-1}.

closed area percolation, compared with Figs. 12(a) and 12(c). Such effect has been reported previously by HS and that's why one need to tune $\Delta(x)$ with observational data.

APPENDIX C: GINZBURG-LANDAU PHASE DIAGRAMS

The study of the Ginzburg-Landau time-dependent equation requires considering the effects of the linear and nonlinear parameters in the phase formation and transition. Represented in the main text as E and K, the polynomial terms in Eq. (11) were explored systematically by identifying two limits: (1) when E and K tend to 0 with results close to the Hottovy and Stechmann outputs and, (2) when E and K increase. In the phase diagram, this produces the formation of symmetry with respect to an intermediate D value, as shown in Figs. 13 and 14.
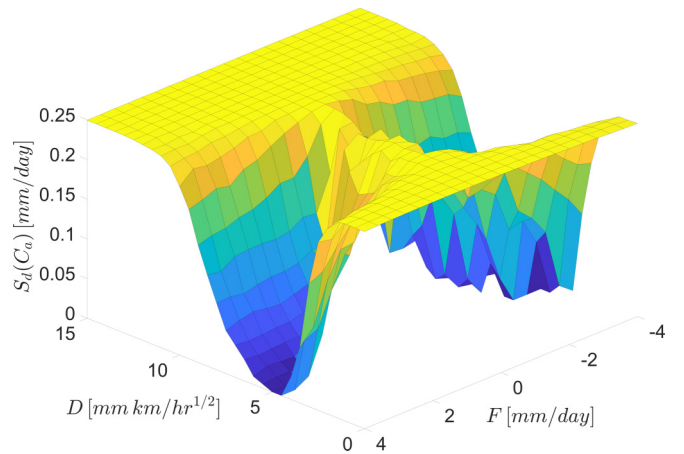
FIG. 14. Plot of the cloud area fraction standard deviation ($S_d(C_a)$) as a function of the D and F, for the Ginzburg-Landau stochastic model given by Eq. (11), fixing the parameters $E = 8.5$ h^{-1} and $K = 6.5$ mm^2 h^{-1}.

[1] T. Schneider, J. Teixeira, C. S. B. F. Brient, K. G. Pressel, C. Schär, and A. P. Siebesma, Climate goals and computing the future of clouds, Nat. Clim. Change **7**, 3 (2017).

[2] L. Nuijens and A. P. Siebesma, Boundary layer clouds and convection over subtropical oceans in our current and in a warmer climate, Curr. Clim. Change Rep. **5**, 80 (2019).

[3] A. Deng, N. L. Seaman, and J. S. Kain, A shallow-convection parametrization for mesoscale models. Part I: Submodel description and preliminary applications, J. Atmos. Sci. **60**, 34 (2002).

[4] S. Rasp, H. Schulz, S. Bony, and B. Stevens, Combining crowdsourcing and deep learning to explore the mesoscale organization of shallow convection, Bull. Am. Meteorol. Soc. **101**, E1980 (2020).

[5] G. Dagan, I. Koren, O. Altaratz, and G. Feingold, Feedback mechanisms of shallow convective clouds in a warmer climate as demonstrated by changes in buoyancy, Environ. Res. Lett. **13**, 054033 (2018).

[6] P. Ceppi, F. Brient, M. D. Zelinka, and D. L. Hartmann, Cloud feedback mechanisms and their representation in global climate models, WIREs Clim. Change **8**, e465 (2017).

[7] B. Khouider and A. Bihlo, A new stochastic model for the boundary layer clouds and stratocumulus phase transition regimes: Open cells, closed cells, and convective rolls, J. Geophys. Res. Atmos. **124**, 367 (2019).

[8] S. B. I. Tobin and R. Roca, Observational evidence for relationships between the degree of aggregation of deep convection, water vapor, surface fluxes, and radiation, J. Clim. **25**, 6885 (2012).

[9] Robert A. Houze Jr., *Cloud Dynamics* (Elsevier B.V., Oxford, UK, 1998).

[10] R. Vogel, L. Nuijens, and B. Stevens, Influence of deepening and mesoscale organization of shallow convection on stratiform cloudiness in the downstream trades, Q. J. R. Meteorol. Soc. **146**, 174 (2019).

[11] R. Wood and J. P. Taylor, Liquid water path variability in unbroken marine stratocumulus cloud, Q. J. R. Meteorol. Soc. **127**, 2635 (2001).

[12] T. Schneider, M. K. Colleen, and K. G. Pressel, Possible climate transitions from breakup of stratocumulus decks under greenhouse warming, Nat. Geosci. **12**, 164 (2019).

[13] R. Wood, Review: Stratocumulus clouds, Mon. Weather Rev. **140**, 2373 (2012).

[14] S. Noteboom, *Open Cell Convection and Closed Cell Convection* (KNMI, De Bilt, 2006).

[15] E. M. Agee, T. S. Chen, and K. E. Dowell, A review of mesoscale cellular convection, Bull. Am. Meteorol. Soc. **54**, 1004 (1973).

[16] C. S. Bretherton and P. N. Blossey, Understanding mesoscale aggregation of shallow cumulus convection using large-eddy simulation, J. Adv. Model. Earth Syst. **9**, 2798 (2017).

[17] S. Hottovy and S. N. Stechmann, A spatiotemporal stochastic model for tropical precipitation and water vapor dynamics, J. Atmosferic Sci. **72**, 4721 (2015).

[18] I. L. McCoy, R. Wood, and J. K. Fletcher, Identifying meteorological controls on open and closed mesoscale cellular convection associated with marine cold air outbreaks, J. Geophys. Res. Atmos. **122**, 11,678 (2017).

[19] G. Feingold, I. Koren, T. Yamaguchi, and J. Kazil, On the reversibility of transitions between closed and open cellular convection, Atmos. Chem. Phys. **15**, 7351 (2005).

[20] T. Yamaguchi and G. Feingold, On the relationship between open cellular convective cloud patterns and the spatial distribution of precipitation, Atmos. Chem. Phys. **15**, 237 (2015).

[21] O. Peters, J. D. Neelin, and S. W. Nesbitt, Mesoscale convective systems and critical clusters, J. Atmosferic Sci. **66**, 2913 (2009).

[22] F. Glassmeiera and G. Feingold, Network approach to patterns in stratocumulus clouds, Proc. Natl. Acad. Sci. USA **114**, 10578 (2017).

[23] P. Bak, C. Tang, and K. Wiesenfeld, Self-organized criticality, Phys. Rev. A **38**, 364 (1988).

[24] O. Peters and J. D. Neelin, Critical phenomena in atmospheric precipitation, Nat. Phys. **2**, 393 (2006).

[25] S. Hottovy and S. N. Stechmann, Cloud regimes as phase transitions, Geophys. Res. Lett. **43**, 6579 (2016).

[26] B. Stevens, G. Vali, K. Comstock, R. Wood, M. van Zanten, P. Austin, C. Bretherton, and D. Lenschow, Pockets of open cells (POCs) and drizzle in marine stratocumulus, Bull. Am. Meteorol. Soc. **86**, 51 (2005).

[27] F. Ahmed and C. Schumacher, Convective and stratiform components of the precipitation-moisture relationship, Geophys. Res. Lett. **42**, 10,453 (2015).

[28] G. C. Craig and J. M. Mack, A coarsening model for self-organization of tropical convection, J. Geophys. Res. Atmos. **118**, 8761 (2013).

[29] S. M. Allen and J. W. Cahn, A microscopic theory for antiphase boundary motion and its application to antiphase domain coarsening, Acta Metall. **27**, 1085 (1979).

[30] J. M. S. Jordi García-Ojalvo, *Noise in Spatially Extended Systems*, 1st ed. (Springer-Verlag, New York, 1999).

[31] M. Loecher, *Noise Sustained Patterns: Fluctuations and Nonlinearities*, 1st ed., World Scientific Lecture Notes in Physics, Vol. 70 (World Scientific, Singapore, 2003).

[32] A. K. Betts and M. J. Miller, A new convective adjustment scheme. Part II: Single column tests using GATE wave, BOMEX, ATEX and arctic air-mass data sets, Q. J. R. Meteorol. Soc. **112**, 693 (1986).

[33] A. J. Majda and M. J. Grote, Mathematical test models for superparametrization in anisotropic turbulence., Proc. Natl. Acad. Sci. USA **106**, 5470 (2009).

[34] S. V. Gurevich, *Numerical Methods for Complex Systems II* (Westfälische Wilhelms-Universität, Münster, Germany, 2017).

[35] S. N. Stechmann and J. D. Neelin, A stochastic model for the transition to stong convection, J. Atmos. Sci. **68**, 2955 (2011).

[36] C. E. Holloway and J. D. Neelin, Moisture vertical structure, column water vapor, and tropical deep convection, J. Atmos. Sci. **66**, 1665 (2009).

[37] C. S. Bretherton, M. E. Peters, and L. E. Back, Relationships between water vapor path and precipitation over the tropical oceans, J. Clim. **17**, 1517 (2004).

[38] J.-I. Yano, C. Liu, and M. W. Moncrieff, Self-organized criticality and homeostasis in atmospheric convective organization, J. Atmos. Sci. **69**, 3449 (2012).

[39] M. D. Lebsock, T. S. L'Ecuyer, and R. Pincus, An observational view of relationships between moisture aggregation, cloud, and radiative heating profiles, Surv. Geophys. **38**, 1237 (2017).

[40] C. E. Holloway and J. D. Neelin, Temporal relations of column water vapor and tropical precipitation, J. Atmos. Sci. **67**, 1091 (2010).

[41] J. J. Binney, N. J. Dowrick, A. J. Fisher, and M. E. J. Newman, *The Theory of Critical Phenomena: An Introduction to the Renormalization Group* (Oxford Science, Oxford, 1992), Chap. 7.

[42] N. Komin, L. Lacasa, and R. Toral, Critical behavior of a Ginzburg-Landau model with additive quenched noise, J. Stat. Mech.: Theory Exp. (2010) P12008.

[43] L. Ramírez-Piscina, J. M. Sancho, and A. Hernández-Machado, Multiplicative noise in domain growth: Stochastic Ginzburg-Landau equations, Phys. Rev. B **48**, 125 (1993).

[44] J. M. Yeomans, *Statistical Mechanics of Phase Transitions* (Oxford Science, Oxford, 1992).

[45] N. W. Watkins, G. Pruessner, S. C. Chapman, N. B. Crosby, and H. J. Jensen, 25 years of self-organized criticality: Concepts and controversies, Space Sci. Rev. **198**, 3 (2016).

[46] D. Jeong, S. Lee, D. Lee, J. Shin, and J. Kim, Comparison study of numerical methods for solving the Allen-Cahn equation, Comput. Mater. Sci. **111**, 131 (2016).

[47] J. Q. Toledo-Marín, I. P. Castillo, and G. G. Naumis, Minimal cooling speed for glass transition in a simple solvable energy landscape model, Physica A **451**, 227 (2016).

[48] J. Q. Toledo-Marín and G. G. Naumis, Short time dynamics determine glass forming ability in a glass transition two-level model: A stochastic approach using Kramers' escape formula, J. Chem. Phys. **146**, 094506 (2017).

[49] R. Kerner and G. G. Naumis, Stochastic matrix description of the glass transition, J. Phys.: Condens. Matter **12**, 1641 (2000).

[50] H. M. Flores-Ruiz, G. G. Naumis, and J. C. Phillips, Heating through the glass transition: A rigidity approach to the boson peak, Phys. Rev. B **82**, 214201 (2010).

[51] A. Huerta and G. G. Naumis, Evidence of a glass transition induced by rigidity self-organization in a network-forming fluid, Phys. Rev. B **66**, 184204 (2002).

[52] G. G. Naumis, Simple solvable energy-landscape model that shows a thermodynamic phase transition and a glass transition, Phys. Rev. E **85**, 061505 (2012).

[53] M. D. Ryser, N. Nigam, and P. F. Tupper, On the well-posedness of the stochastic Allen-Cahn equation in two dimensions, J. Comput. Phys. **231**, 2537 (2012).

[54] R. Krishnamurti, On cellular cloud patterns. Part 1: Mathematical model, J. Atmos. Sci. **32**, 1353 (1975).

[55] M. Cross, *Lecture 8 Supplementary Notes: Amplitude Equations* (Beijing Normal University, Beijing, China, 2006).

[56] M. van Hecke, P. C. Hohenberg, and W. van Saarloos, Amplitude equations for pattern forming systems, in *Fundamental Problems in Statistical Mechanics*, Vol. VIII, edited by H. van Beijeren and M. H. Ernst (North Holland, Amsterdam, 1994), pp. 245–278.

[57] J. Swift and P. C. Hohenberg, Hydrodynamic fluctuations at the convective instability, Phys. Rev. A **15**, 319 (1977).

[58] P. Gao, The stochastic Swift–Hohenberg equation, Nonlinearity **30**, 3516 (2017).

[59] J. García-Ojalvo, A. Hernández-Machado, and J. M. Sancho, Effects of External Noise on the Swift-Hohenberg Equation, Phys. Rev. Lett. **71**, 1542 (1993).

[60] S. S. Pérez-Moreno, M. S. R. Chavarría, and G. Ruiz-Chavarría, Numerical solution of the swift-hohenberg equation, in *Experimental and Computational Fluid Mechanics: Environmental Science and Engineering*, edited by J. Klapp and A. Medina (Springer, Berlin, 2014), pp. 409–416.